



**Lattice Boltzmann model for predicting frosting process on surfaces considering wettability**Shusheng Zhang <sup>1</sup>, Taiping Jiang,<sup>1</sup> Hai Huang,<sup>2</sup> Lin-Jie Huang,<sup>2</sup> and Li-Zhi Zhang <sup>1,3,\*</sup><sup>1</sup>Key Laboratory of Enhanced Heat Transfer and Energy Conservation of Education Ministry, School of Chemistry and Chemical Engineering, South China University of Technology, Guangzhou 510640, China<sup>2</sup>Sanhua Holding Group, Hangzhou 310000, China<sup>3</sup>State Key Laboratory of Subtropical Building Science, South China University of Technology, Guangzhou 510640, China

(Received 1 March 2022; revised 9 March 2023; accepted 9 May 2023; published 22 June 2023)

The process of frosting is a multiscale problem, which leads to challenges of proposing accurate numerical methods. In this study, a lattice Boltzmann model for predicting frost formation and growth on surfaces of various wettabilities is proposed based on the heterogeneous nucleation and dendrite growth theories. Three lattice Boltzmann equations are used to calculate the velocity, humidity, and temperature distributions. Furthermore, the heterogeneous nucleation theory and dendrite growth theory are used to construct the equations that govern ice production during the frosting process, so that the surface wettability can be considered. After experimental validation, the model was used in the analysis of frosting behaviors on plates and in microchannels with different wettabilities. The effects of the intrinsic contact angles and roughness on the frost layer properties were evaluated. This study will likely facilitate a better understanding of frosting on the mesoscopic level.

DOI: [10.1103/PhysRevE.107.065304](https://doi.org/10.1103/PhysRevE.107.065304)**I. INTRODUCTION**

Frost formation and growth on cold surfaces are common phenomena in food processing, the aerospace industry, refrigeration, and air conditioning. Unfortunately, frosting usually results in potential safety hazards, high flow resistance, and thermal performance degradation. Therefore, many defrosting and antifrosting studies have been conducted to alleviate the limitations introduced by frost [1–3]. A key issue in these studies is the exploration of the mechanisms associated with frost formation and growth. However, it is very difficult to study the rules of complex frosting processes based on experimental and theoretical analyses. Fortunately, rapid advances in the field of numerical simulation have been realized over the past 30 years. As such, the mechanisms of the frosting process can be investigated using computer simulation. Naturally, an accurate mathematical model should be proposed first to take advantages of numerical simulation.

The development of a mathematical model to describe the frosting process is relevant to a wide range of fields. In recent years, several frosting models have been proposed. In general, the physical domain of the frosting process can be divided into a humid air region and a porous frost layer. Lei *et al.* [4] divided the existing frosting models into three groups according to the equations that govern the frosting process. In the first group, the governing equations were established for only the frost layer, and the properties of the humid air region were calculated using empirical correlations [5,6]. In the second group, the governing equations were established for the humid air region and the porous frost layer [7–9]. The connection between these two subdomains was calculated using additional

air-frost interfacial conditions, but the convection effect was ignored in the frost layer. In the third group, the governing equations of the humid air region and porous frost layer were proposed for the entire frosting region. Different calculation methods were used to describe the mass transfer rate from the air to the ice phase [10,11], and the deficiencies of the first two groups can be addressed. Though more accurate, these models still do not describe the effects of the substrate plates. Many experimental studies have shown that the wettability of plates, which is related to roughness, can significantly affect the physical properties of the frost layer [12–15]. However, the effects of the wettability of the plates during the frosting processes have been ignored in previous numerical simulation studies [2,3,16]. Although the current mathematical models can be used to predict the effects of the wet air properties such as air velocity and relative humidity on frost layer properties, they fail to predict the effects of substrate wettability during the frosting process.

To solve this problem, an interfacial mass-transfer scheme was proposed based on the modified heterogeneous nucleation theory and dendrite growth theory to describe the formation of frost layers on the surfaces with different wettabilities. Moreover, in frosting processes, the frost layer is generally considered to be a porous medium. In addition to the conventional computational fluid dynamics model [17–19], lattice Boltzmann method (LBM) is an effective approach for the treatment of complex boundaries because of its flexibility. Therefore, in this study, the physical fields of frosting process were calculated using a generalized lattice Boltzmann model proposed by Lei *et al.* [4] to simultaneously simulate the frosting properties in both the humid air and the frost layer.

In summary, whereas many studies have been conducted to develop models for frosting calculations, few have considered the wettability of cold surfaces. To address this limitation, a

\*Corresponding author: [lzzhang@scut.edu.cn](mailto:lzzhang@scut.edu.cn)

mathematical model for predicting frost formation and growth on surfaces with various wettabilities is proposed based on nucleation and dendrite growth theories. The intrinsic contact angle and roughness are key factors that influence wettability, in the name of apparent contact angle. Therefore, the model first considers the effects of the intrinsic contact angle. The roughness is then generated on the surfaces, and the consequent frosting is simulated. This report consists of five themed sections. In Sec. I, the background of the study is briefly introduced. Section II is an overview of the methodology. Section III introduces the experimental setup of the frosting process that was used to evaluate the mathematical model. The results of the research and the discussion of the results are presented in Sec. IV. Finally, a summary is provided in Sec. V.

## II. THEORETICAL MODELS

### A. Generalized governing equations for fluids in a porous frost layer

During frosting, the frost layer can be regarded as a porous medium with a variable porosity  $\varepsilon$  consisting of an ice matrix and air gaps [4]. In general, three scales can be involved during flow in porous media, including the pore scale, the representative elementary volume (REV) scale, and the domain scale [20]. Given the complex porous structure of frost, the volume-averaging procedure is usually used to model the flow in a porous frost layer at the representative elementary volume scale [21]. In the elementary control volume  $V$ , the volume fraction of the  $k$ th phase ( $f_k$ ) in a porous medium can be calculated by the ratio of the volume of the  $k$ th phase ( $V_k$ ) to the total elementary control volume [21]:

$$f_k = \frac{V_k}{V}. \quad (1)$$

In this study, the humid air and ice coexist in elementary control volume. Then, the volume fractions of wet air and frost are defined as follows [21]:

$$f_a = \varepsilon = \frac{V_a}{V}, \quad f_s = \frac{V_s}{V} = 1 - f_a. \quad (2)$$

The subscripts ‘‘a’’ and ‘‘s’’ represent the properties of the wet air and solid ice phase, respectively. It can be seen from Eq. (2) that  $f_a=1$  and  $f_a=0$  for pure humid air and a pure ice phase, respectively;  $0 < f_a < 1$  for porous frost layer. Herein,  $\varepsilon$  is also used to denote the volume fractions of wet air (or porosity).

The volume-averaged physical quantity  $\chi$  in an elementary control volume can be expressed as follows [21]:

$$\chi = \chi_s f_s + \chi_a f_a. \quad (3)$$

The volume-averaged velocity, pressure, temperature, and humidity can be calculated by Eq. (3).

During frost formation and growth on cold surfaces, the continuity equation, the generalized non-Darcy equation, and the energy and species conservation equations at the REV scale can be expressed as follows [20,21]:

$$\rho_a \frac{\partial \varepsilon}{\partial t} + \rho_a \nabla \cdot \mathbf{u} = -\dot{m}, \quad (4)$$

$$\rho_a \frac{\partial \mathbf{u}}{\partial t} + \rho_a \mathbf{u} \cdot \nabla \left( \frac{\mathbf{u}}{\varepsilon} \right) = -\nabla(\varepsilon p) + \rho_a v_e \nabla^2 \mathbf{u} + \rho_a \mathbf{F} + \mathbf{M}, \quad (5)$$

$$\omega \frac{\partial T}{\partial t} + \mathbf{u} \cdot \nabla T = \frac{1}{\rho_a c_{p,a}} \nabla \cdot (k_a \nabla T) - \frac{H_{sg}}{c_{p,a}} \frac{\partial \varepsilon}{\partial t}, \quad (6)$$

$$\varepsilon \frac{\partial W_v}{\partial t} + \mathbf{u} \cdot \nabla W_v = D_e \nabla^2 W_v - \frac{\dot{m}}{\rho_a}, \quad (7)$$

where  $\mathbf{u}$ ,  $p$ ,  $T$ , and  $W_v$  are the volume-averaged velocity, pressure, temperature, and humidity, respectively.  $\rho_a$  is the density of humid air,  $\dot{m}$  is mass-transfer source during frosting process.  $v_e$  and  $D_e$  are the effective values of kinematic viscosity and diffusion coefficients, respectively.  $k_a$  and  $c_p$  are the thermal conductivity and specific heat at constant pressure, respectively.  $H_{sg}$  is the latent heat.  $\omega$  is the heat capacity ratio, which is calculated as follows [21]:

$$\omega = \frac{\rho_a c_{p,a} \varepsilon + \rho_s c_{p,s} f_s}{\rho_a c_{p,a}}. \quad (8)$$

The  $\mathbf{F}$  and  $\mathbf{M}$  in Eq. (5) are defined as the total body force and the momentum transfer rate in the frosting process, respectively. The total body force is calculated as [20]

$$\mathbf{F} = -\frac{\varepsilon v_a}{K} \mathbf{u} - \frac{\varepsilon F_\varepsilon}{\sqrt{K}} |\mathbf{u}| \mathbf{u} + \varepsilon \mathbf{G}, \quad (9)$$

where  $v_a$  is defined as the kinematic viscosity of humid air, and  $\mathbf{G}$  is an external force such as gravity. The geometric function  $F_\varepsilon$  and permeability  $K$  were calculated as follows [22,23]:

$$F_\varepsilon = \frac{1.75}{\sqrt{150\varepsilon^3}}, \quad K = \frac{\varepsilon^3 d_m^2}{150(1-\varepsilon)^2}, \quad (10)$$

where  $d_m$  is defined as ice droplet diameter.

### B. Heterogeneous nucleation theory and dendrite growth theory

There has been significant progress in the understanding of frost growth based on the work of Hayashi *et al.* [24]. According to previous studies [3,24], the frosting process can be divided into the crystal growth period, frost-layer growth period, and frost-layer full-growth period. During the crystal growth and the frost-layer growth periods, the nucleation and dendrite growth of ice crystals result in a continuous increase in the frost-layer thickness and density. Moreover, in the frost-layer full-growth period, the upper part of the frost layer melts into water owing to the release of latent heat. The water penetrates the frost layer and freezes on the cold surface, resulting in compact ice. Based on the research of Hayashi *et al.* [24], the mass transfer in the frost full-growth period is much less compared to that of the crystal growth and the frost-layer growth periods. Furthermore, the effects of wettability on the frosting process are mainly reflected in the initial frost formation [25]. Therefore, the frost-layer full-growth period was neglected in this study. Frosting formation is simplified into two processes to investigate the effects of wettability. The first is the process of ice crystal formation and growth, and the other is the process of dendrite growth. A diagram of the two simplified processes is shown in Fig. 1.

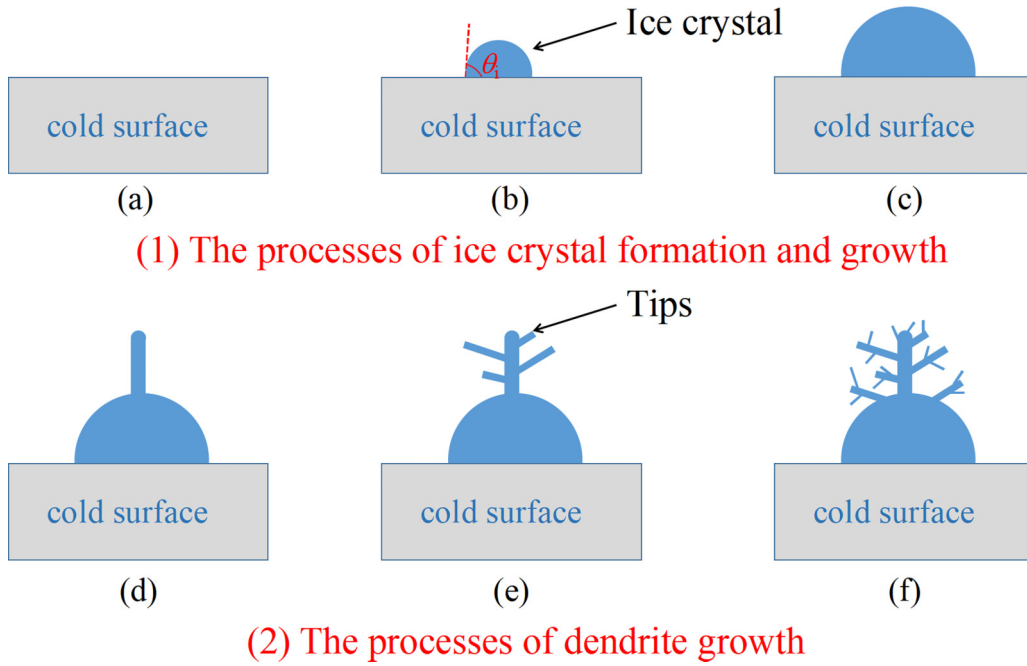


FIG. 1. Diagram of the two simplified processes that occur during the frosting process.

During the frosting process, the volume fraction of the ice phase  $f_s$  continues to increase. Ice generation is closely related to the mass-transfer source term  $\dot{m}$ . It can be represented as follows:

$$\rho_s \frac{\partial f_s}{\partial t} = \dot{m}, \tag{11}$$

where  $\rho_s$  is the ice density. Therefore, the mass-transfer source term is a key factor in the frosting process.

As shown in Fig. 1, during the frosting formation, the increase in the mass of frost involves three components: the formation of ice crystals [Fig. 1(b)], the ice crystal growth [Fig. 1(c)], and dendrite growth [Figs. 1(d)–1(f)]. These three components can be defined as  $m_1$ ,  $m_2$ , and  $m_3$ , respectively. The  $\theta_i$  in Fig. 1(b) denotes the intrinsic contact angle of the cold surface, which represents the properties of the material.

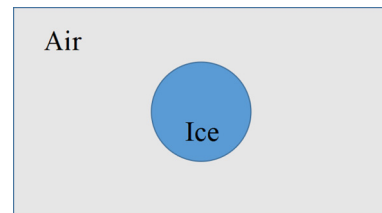
Then, the mathematical expression for mass-transfer source  $\dot{m}$  can be described as follows:

$$\dot{m} = m_1 + m_2 + m_3. \tag{12}$$

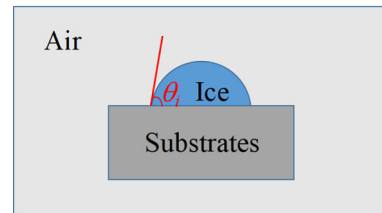
The process of ice crystal formation and growth [Fig. 1, (1)] is similar to that of condensation. The results of previous studies have shown that this process can be described using nucleation theory [26–29]. Nucleation refers to the formation of crystal nuclei during the initial stage of crystallization. Typically, nucleation processes can be divided into homogeneous nucleation and heterogeneous nucleation, depending on whether the process is promoted by the presence of foreign bodies [30]. Foreign bodies may be substrates or particles. The presence of foreign bodies reduces the surface energy and then reduces the nucleation barrier. Therefore, nucleation preferentially occurs on foreign bodies in a process known as heterogeneous nucleation [30]. However, most previous numerical studies assume that homogeneous nucleation occurs in the computational domain for convenience. Thus, the

existing calculation methods for the interfacial mass-transfer rate based on the homogeneous nucleation theory should be improved to consider dominant heterogeneous nucleation associated with foreign bodies such as heterogeneous plates.

As shown in Fig. 2, the shapes of ice nuclei formed via the two nucleation mechanisms are different. The ice nuclei formed by homogeneous nucleation are spherical, whereas those formed by heterogeneous nucleation can be considered to be segments. Then, the interfacial mass transfer of heterogeneous nucleation can then be analogized to that of homogeneous nucleation [27,29]. According to the formula for the calculation of the area of a segment,  $m_1$  can be calculated



(a) Homogeneous nucleation



(b) Heterogeneous nucleation

FIG. 2. Diagram of homogeneous nucleation and heterogeneous nucleation.

as follows:

$$m_1 = \frac{1}{3}\pi\rho_s J r_c^3 (2 + \cos\theta_i)(1 - \cos\theta_i)^2, \quad (13)$$

where  $J$  and  $r_c$  are used to denote the nucleation rate and critical radius of the ice crystal, respectively, and  $\theta_i$  denotes the intrinsic contact angle. In fact, the roughness of surfaces has a significant influence on the wettability. Therefore, the difference between the apparent contact angle  $\theta_a$  and intrinsic contact angle  $\theta_i$  should be distinguished. Generally, the contact angle, which can be determined experimentally, is the apparent contact angle. Before the numerical calculation can be performed using the presented model, it must be transformed into an intrinsic contact angle. The relation can be described as [31]

$$\cos\theta_a = \beta \cos\theta_i, \quad (14)$$

where  $\beta$  is the roughness factor. It is defined as the ratio of the area of the rough surface to the area of the smooth surface.

In Eq. (13), the critical radius of the ice crystal  $r_c$  is calculated as follows [32]:

$$r_c = \frac{2\sigma T_{\text{sat}}}{\rho_s H_{\text{sg}}(T_{\text{sat}} - T)}. \quad (15)$$

The water vapor saturation temperature  $T_{\text{sat}}$  is related to humidity. The interfacial energy between ice and air  $\sigma$  can be calculated as [29]

$$\sigma = (99.5 - 0.075T) \times 10^{-3}. \quad (16)$$

The nucleation rate  $J$  in Eq. (13) is obtained from classical nucleation theory as follows [26]:

$$J = J_0 \exp\left(-\frac{\pi\sigma r_c^2(2 + \cos\theta)(1 - \cos\theta)^2}{3k_B T}\right), \quad (17)$$

where  $k_B$  is the Boltzmann constant. The kinetic constant of the nucleation rate  $J_0$  can be expressed as [33]

$$J_0 = \frac{n_c}{1 + \zeta} \left(\frac{\rho_v^2}{\rho_s}\right) \sqrt{\frac{2\sigma}{M^3\pi}}, \quad (18)$$

where  $\rho_v$  is the vapor density, and the water molecular mass  $M = 2.989 \times 10^{-26}$  kg is used throughout the simulation process, where  $n_c$  is the nucleation coefficient. The nonisothermal correction factor  $\zeta$  is calculated as follows [34]:

$$\zeta = \frac{2(\gamma - 1)H_{\text{sg}}}{(\gamma + 1)RT} \left(\frac{H_{\text{sg}}}{RT} - 0.5\right), \quad (19)$$

where  $\gamma = 1.32$  is the specific heat capacity ratio, and  $R = 461.4$  J/(kg K) is the universal gas constant.

We then consider the addition of mass from ice crystal growth (when  $r > r_c$ ). As the ice crystals grow, an average radius of the ice crystals is assumed. As the average radius  $\bar{r}$  increases, the mass of the ice crystals also increases. This is analogous to homogeneous nucleation [34]. Based on the formula for the surface area of a spherical cap,  $m_2$  can be represented as

$$m_2 = (2\pi\bar{r}^2(1 - \cos\theta))\rho_s N \frac{d\bar{r}}{dt}, \quad (20)$$

where  $N$  is the number of ice crystals per unit volume, which can be calculated as follows:

$$N = \sum_i J(t). \quad (21)$$

The ice crystal growth rate  $d\bar{r}/dt$  can be estimated from the energy balance around the segment. It can be expressed as

$$\frac{d\bar{r}}{dt} = \frac{2(1 - \cos\theta_i)h_v(T_{\text{sat}} - T)(1 - \frac{r_c}{\bar{r}})}{\rho_s H_{\text{sg}}(2 + \cos\theta_i)(1 - \cos\theta_i)^2}. \quad (22)$$

The heat-transfer coefficient  $h_v$  can be calculated as follows [34]:

$$h_v = \frac{\lambda_v}{\bar{r}(1 + 3.18\text{Kn})}, \quad (23)$$

where  $\lambda_v$  is the thermal conductivity of vapor.

Therefore, the ice crystal growth rate can be described as

$$\frac{d\bar{r}}{dt} = \frac{2(1 - \cos\theta_i)\lambda_v(T_{\text{sat}} - T)(1 - \frac{r_c}{\bar{r}})}{(2 + \cos\theta_i)(1 - \cos\theta_i)^2\rho_s H_{\text{sg}}\bar{r}(1 + 3.18\text{Kn})}. \quad (24)$$

The Knudsen number  $\text{Kn}$  is defined as

$$\text{Kn} = \frac{\bar{l}}{2\bar{r}}, \quad (25)$$

where  $\bar{l}$  is the mean-free path of vapor molecules, which can be calculated by [35]

$$\bar{l} = \frac{3\mu_v\sqrt{RT}}{2p}, \quad (26)$$

where  $\mu_v$  is the vapor dynamic viscosity.

The process of dendrites growth [Fig. 1, (2)] can be described using the dendrite growth theory, which has been widely used in the field of metallic dendrite growth [36,37]. The results of many studies have shown that dendrite growth is very similar during the frosting process and the growth of metallic dendrites [38,39]. Both are due to the diffusion of tips caused by local supercooling [40]. The process of dendrite growth can be analyzed on a mesoscopic scale using the classical Lipton-Glicksman-Kurz(LGK)/Lipon-Kurz-Trivedi(LKT) model [40,41]. According to this model, the dendrite growth velocity  $v_d$  and dendrite tip radius  $R_d$  can be calculated as follows:

$$v_d = \frac{1}{\eta_k} \left(T_{\text{mp}} - T_{\text{if}} + \frac{2\Gamma}{R_d}\right), \quad (27)$$

$$R_d = \frac{\Gamma}{\phi T_{\text{mp}} \text{Pe}_g}, \quad (28)$$

where  $\eta_k$  is the interfacial kinetic coefficient, and  $\Gamma$  is the Gibbs-Thompson coefficient.  $T_{\text{mp}}$  and  $T_{\text{if}}$  are the melting temperature and interface temperature of the dendrites, respectively. Furthermore,  $\phi$  is the stability parameter,  $\text{Pe}_g$  is the thermal Peclet number. In this study, dendrite growth is considered to begin when the ice-volume fraction is greater than  $10^{-6}$ . This value is used to determine when the frosting process enters the dendrite growth period [27,42].

Furthermore, all dendrites are assumed to be cylindrical. The addition of mass owing to dendrite growth can be

described as follows:

$$m_3 = \pi R_d^2 v_d \rho_s. \quad (29)$$

### C. Lattice Boltzmann models

In this study, the generalized LBM was employed to simulate the velocity field, humidity field, and temperature field [4,20], because of the flexibility in dealing with complex boundary geometries and the mesoscale nature of LBM.

The lattice Boltzmann equation of fluid flow can be expressed as [4]

$$\begin{aligned} & f_i(\mathbf{x} + \mathbf{e}_i \delta_t, t + \delta_t) - f_i(\mathbf{x}, t) \\ &= -\frac{1}{\tau_u} [f_i(\mathbf{x}, t) - f_i^{\text{eq}}(\mathbf{x}, t)] + \delta_t F_i + \delta_t R_i, \end{aligned} \quad (30)$$

where  $f_i$  is the velocity distribution function. The dimensionless relaxation time  $\tau_u$  can be calculated by [4]

$$\tau_u = \frac{v_e}{c_s^2 \delta_t} + \frac{1}{2}, \quad (31)$$

where effective kinematic viscosity is calculated by

$$v_e = W_v v_v + (1 - W_v) v_a, \quad (32)$$

where  $v_v$  denotes the kinematic viscosity of water steam.

The  $c_s = e/\sqrt{3}$  is the lattice sound velocity;  $\delta_t$  is the time step. The equilibrium distribution function  $f_i^{\text{eq}}$  can be defined as

$$f_i^{\text{eq}} = w_i \left\{ \rho_p + \rho_a \left[ \frac{\mathbf{e}_i \cdot \mathbf{u}}{c_s^2} + \frac{\mathbf{u} \mathbf{u} : (\mathbf{e}_i \mathbf{e}_i - c_s^2 \mathbf{I})}{2 \varepsilon c_s^4} \right] \right\}, \quad (33)$$

where  $\rho_p$  is defined as  $\rho_p = \varepsilon p / c_s^2$ , and  $\mathbf{I}$  is the unit tensor. This equilibrium distribution for incompressible fluid flows can reduce compressible errors [4,43].

For present research, the two-dimensional, nine-velocity (D2Q9) and three-dimensional, nineteen-velocity (D3Q19) LBM are applied for two-dimensional and three-dimensional study, respectively. The discrete velocity  $\mathbf{e}_i$  and weight coefficient  $w_i$  for different directions can be defined as for a two-dimensional study [44]:

$$\mathbf{e}_i = \begin{cases} (0, 0) & i = 0 \\ (\pm 1, 0) \frac{\delta x}{\delta t}, (0, \pm 1) \frac{\delta x}{\delta t} & i = 1 \sim 4, \\ (\pm 1, \pm 1) \frac{\delta x}{\delta t} & i = 5 \sim 8 \end{cases} \quad (34)$$

$$w_i = \begin{cases} 4/9 & i = 0 \\ 1/9 & i = 1 \sim 4. \\ 1/36 & i = 5 \sim 8 \end{cases} \quad (35)$$

Correspondingly, the discrete velocity and weights for three-dimensional study can be defined as [44]

$$\mathbf{e}_i = \begin{cases} (0, 0) & i = 0 \\ (\pm 1, 0, 0) \frac{\delta x}{\delta t}, (0, \pm 1, 0) \frac{\delta x}{\delta t}, (0, 0, \pm 1) \frac{\delta x}{\delta t} & i = 1 \sim 6, \\ (\pm 1, \pm 1, 0) \frac{\delta x}{\delta t}, (0, \pm 1, \pm 1) \frac{\delta x}{\delta t}, (\pm 1, 0, \pm 1) \frac{\delta x}{\delta t} & i = 7 \sim 18 \end{cases} \quad (36)$$

$$w_i = \begin{cases} 1/3 & i = 0 \\ 1/18 & i = 1 \sim 6. \\ 1/36 & i = 7 \sim 18 \end{cases} \quad (37)$$

The distribution function  $F_i$  can be calculated by [4]

$$\begin{aligned} F_i &= w_i \left( 1 - \frac{1}{2\tau_u} \right) \\ &\times \left[ \frac{\mathbf{e}_i \cdot (\rho_l \mathbf{F} + \mathbf{M})}{c_s^2} + \frac{\mathbf{u} (\rho_l \mathbf{F} + \mathbf{M}) : (\mathbf{e}_i \mathbf{e}_i - c_s^2 \mathbf{I})}{\varepsilon c_s^4} \right]. \end{aligned} \quad (38)$$

Furthermore, the distribution function  $R_i$  for mass source  $\dot{m}$  is described as [4]

$$R_i = -w_i \dot{m} \left( 1 - \frac{1}{2\tau_u} \right). \quad (39)$$

The macroscopic density  $\rho$  and velocity  $\mathbf{u}$  can be obtained at each time step, and can be expressed as [4]

$$\rho_p = \sum_i f_i - \frac{\delta t}{2} \dot{m}, \quad (40)$$

$$\rho_a \mathbf{u} = \frac{\mathbf{v}}{c_0 + \sqrt{c_0^2 + c_1 |\mathbf{v}|}}, \quad (41)$$

with auxiliary velocity  $\mathbf{v}$  [4]:

$$\mathbf{v} = \sum_i \mathbf{e}_i f_i + \rho_a \frac{\delta_t}{2} \varepsilon \mathbf{G} + \frac{\delta_t}{2} \mathbf{M}, \quad (42)$$

and two parameters of auxiliary velocity [20]:

$$c_0 = \frac{1}{2} \left( 1 + \varepsilon \frac{\delta_t v_a}{2K} \right), \quad c_1 = \varepsilon \frac{\delta_t F_\varepsilon}{2\sqrt{K}}. \quad (43)$$

For the humidity field, another lattice Boltzmann equation is used to determine the humidity distribution function  $h_i$  as follows [4]:

$$\begin{aligned} & h_i(\mathbf{x} + \mathbf{e}_i \delta_t, t + \delta_t) - h_i(\mathbf{x}, t) \\ &= -\frac{1}{\tau_w} [h_i(\mathbf{x}, t) - h_i^{\text{eq}}(\mathbf{x}, t)] + \delta_t H_i, \end{aligned} \quad (44)$$

where  $\tau_w$  refers to the relaxation time. It is calculated by

$$\tau_w = \frac{D_e}{\varepsilon c_s^2 \delta_t} + \frac{1}{2}, \quad (45)$$

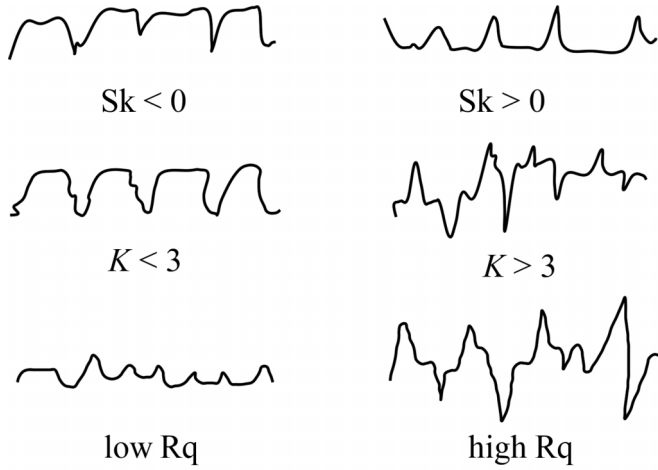


FIG. 3. Schematic diagrams of different roughness parameters.

where effective diffusion coefficient  $D_e$  is obtained by the empirical correlation [6]

$$D_e = D_a \varepsilon \frac{1 + \varepsilon}{2}, \quad (46)$$

where  $D_a$  is the diffusion coefficient of humid air.

The humidity equilibrium distribution  $h_i^{eq}$  is given by

$$h_i^{eq} = w_i W_v \left( \varepsilon + \frac{\mathbf{e}_i \cdot \mathbf{u}}{c_s^2} \right). \quad (47)$$

With regard to  $H_i$ , the source term in Eq. (44) is defined as

$$H_i = -w_i \varepsilon \frac{\dot{m}}{\rho_a}. \quad (48)$$

Furthermore, the mass fraction of water steam is obtained by

$$\varepsilon W_v = \sum_i h_i. \quad (49)$$

Moreover, the lattice Boltzmann equation for temperature distribution function  $g_i$  can be described as [4]

$$g_i(\mathbf{x} + \mathbf{e}_i \delta_t, t + \delta_t) - g_i(\mathbf{x}, t) = -\frac{1}{\tau_t} [g_i(\mathbf{x}, t) - g_i^{eq}(\mathbf{x}, t)] + \delta_t G_i, \quad (50)$$

where  $\tau_t$  is the relaxation time of temperature field. It can be calculated by

$$\tau_t = \frac{\alpha_e}{\omega c_s^2 \delta_t} + \frac{1}{2}, \quad (51)$$

where  $\alpha_e$  is the effective thermal diffusivity.

The temperature equilibrium distribution  $g_i^{eq}$  is given by

$$g_i^{eq} = w_i T \left( \omega + \frac{\mathbf{e}_i \cdot \mathbf{u}}{c_s^2} \right). \quad (52)$$

The source term  $G_i$  is defined as

$$G_i = w_i \omega \frac{H_{sg}}{c_{p,a}} \frac{\partial \varepsilon}{\partial t}. \quad (53)$$

Then, the temperature is calculated by

$$\omega T = \sum_i g_i. \quad (54)$$

So far, the velocity, humidity, and temperature fields of frosting process can be obtained by LBM in this study. The

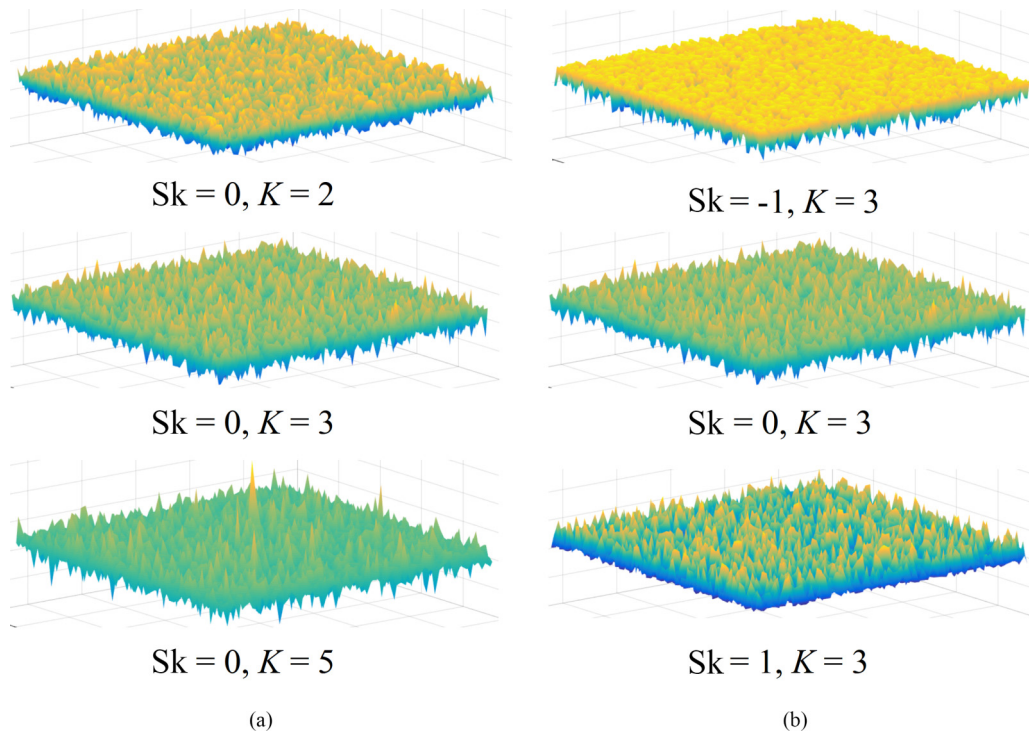


FIG. 4. Rough surface morphology with different roughness parameters: (a) Effects of  $K$ ; (b) effects of  $Sk$ .

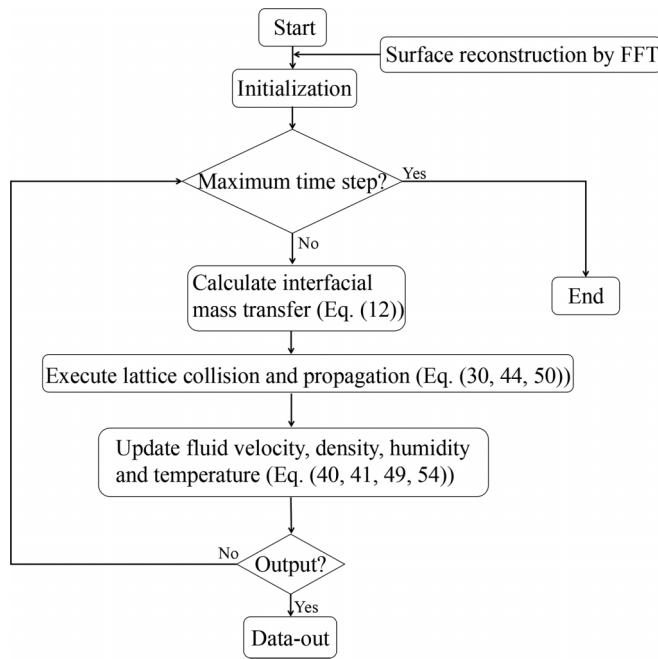


FIG. 5. Flow chart of simulation procedures for predicting the frosting process.

Champan-Enskog technique can be used to recover the governing equations (4)–(7) from lattice Boltzmann equations [4]. It should be noted that the immersed moving-boundary method was used to track the solid-liquid phase-change interface in many previous studies [45–47]. This is more detailed; however, it consumes much computational effort, unaffordable for simulation of a real exchanger microchannel which is modeled in present study. So, this study takes a more large-scale (representative elementary volume scale) approach [4,20,48]. The interface of each ice crystal is not tracked, but their effects are considered by the mass source terms and governing equations through Eqs. (11), (13), (20), and (29). The

phase-change surface is obtained by the change of ice mass fraction in elementary control volume due to energy change by Eqs. (11), (13), (20), and (29). Therefore, the immersed moving-boundary scheme is not employed in Eq. (30).

#### D. Random surface reconstruction algorithm

The roughness of superhydrophobic surfaces is usually randomly distributed. To study the effects of surface roughness, a reconstruction algorithm is utilized in the simulation to build the surface. The random roughness is mainly described by four statistical parameters: mean height, skewness ( $S_k$ ), kurtosis ( $K$ ), and standard deviation ( $R_q$ ). The mean height is the average height of the rough surfaces. Skewness is the degree of skew away from the central distribution. For a randomly rough surface with a Gaussian distribution, the skewness is 0, which means that the peak value and valley value are equal at the height deviation value of the surface. A surface with the peak value removed has a negative skewness, whereas a surface with the valley value removed has a positive skewness. The kurtosis is used to describe the surface roughness distribution of the peak. For a randomly rough surface with a Gaussian distribution, the kurtosis is 3.0. When the kurtosis is higher than 3.0, the surface has more peak and valley values than a Gaussian distribution surface. Relatively, when the kurtosis is lower than 3.0, the surface has fewer peak and valley values compared to a Gaussian distribution surface. The standard deviation measures the degree to which the surface height distribution deviates from the mean height. The fluctuation of the surface roughness is enhanced with an increase in the standard deviation. Figure 3 shows the effects of different skewness, kurtosis, and standard deviations on the surface morphology.

In order to clarify the effects of roughness parameters on surface morphology, five different rough surfaces were reconstructed, including one randomly rough surface with Gaussian distribution ( $S_k = 0, K = 3$ ) and four randomly rough surfaces with non-Gaussian distribution. Figure 4 shows the

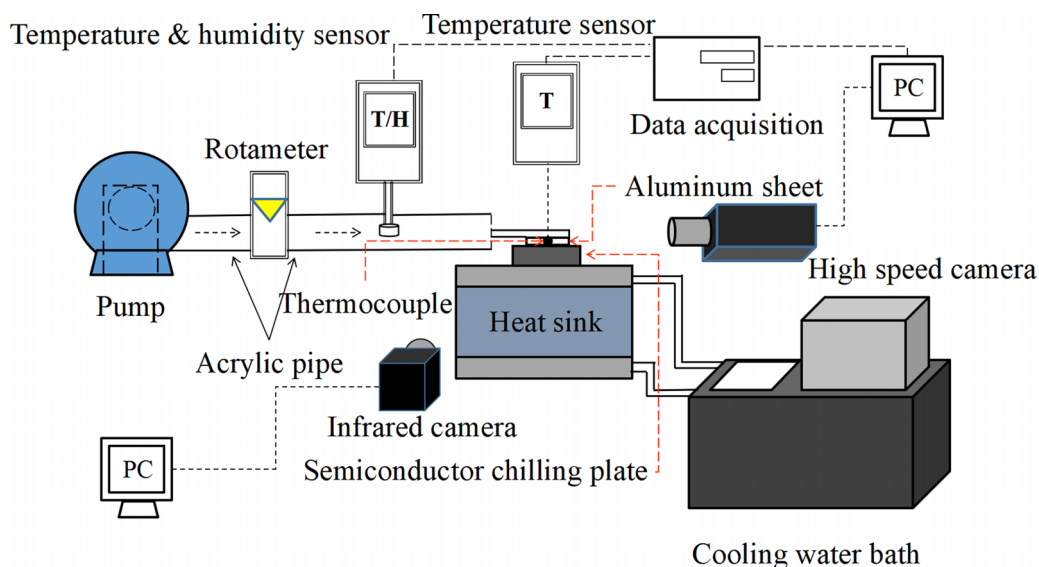


FIG. 6. Schematic diagram of the experimental setup for the frost formation and growth experiments on cold surfaces.

comparison of roughness for the Gaussian and non-Gaussian distributions. As introduced above, when the kurtosis is higher than 3.0, the surface has more peak and valley values than a Gaussian distribution surface does. Relatively, when the kurtosis is lower than 3.0, the surface has fewer peaks and valley values compared to a Gaussian distribution surface does. Moreover, the less peak and valley values are caused by the negative skewness and positive skewness, respectively.

There are various methods for obtaining randomly distributed rough surfaces based on computer reconstruction. In previous studies [49,50], the fast Fourier transform method has been used for this purpose. The details of this method are presented in a previous study [51].

In addition, the following physical assumptions are used to simplify the simulation process: (1) humid air is considered to be an incompressible Newtonian fluid because of its low velocities; (2) the fluctuation of physical parameters with temperature is negligible; (3) the effect of gravity is negligible ( $\mathbf{G}=\mathbf{0}$ ); (4) the velocity of humid air is sufficiently high that natural convection can be ignored; and (5) The temperature of the cold surface is considered to be much lower than the freezing-point temperature, and thus, vapor is directly condensed into frost.

Based on the aforementioned discussion, a flow chart of the procedures based on the proposed mathematical model for predicting frosting processes is shown in Fig. 5.

### III. EXPERIMENT SETUP

To validate the mathematical model proposed in this study, an experimental setup for the study of frost formation and growth on cold surfaces was designed, as shown in Fig. 6. The test rig consisted of three parts: a gas supply system, an imaging and measurement system, and a cooling system. During the experiment, the air pump supplied a moist air stream. Humid air was blown across an aluminum sheet using an acrylic pipe. The cooling of the aluminum sheet was achieved using a semiconductor chilling plate. The hot side of the semiconductor chilling plate was cooled using circulating cooling water piped from a cooling water bath. In addition, the initial temperature and humidity of the wet air were measured using temperature and humidity sensors. The cold-surface temperature was measured by K-type thermocouples embedded on the surface. The humid air velocity was recorded using a rotameter, and the formation and growth of the frost layer were recorded by a high-speed camera. The frost thickness and frost temperature were obtained by the high-speed camera and infrared camera, respectively, to alleviate the influences

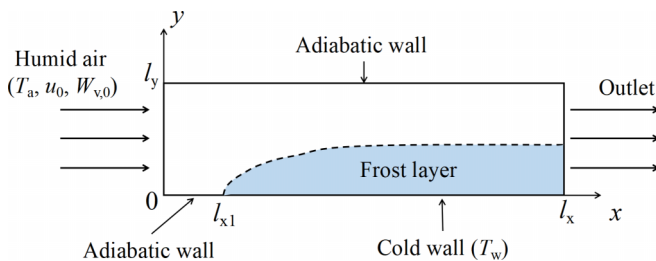


FIG. 7. Computational domain for model validation [4,53].

TABLE I. Physical properties for present study.

Parameter	Dimension	Air	Water vapor	Ice
Density	kg/m <sup>3</sup>	1.293	0.554	915
Kinematic viscosity	m <sup>2</sup> /s	1.322 × 10 <sup>-5</sup>	2.418 × 10 <sup>-5</sup>	
Thermal conductivity	W/(m K)	0.0242	0.0261	2.5
Specific heat	J/(kg K)	1006.43	2014	2100

of sensors on frosting processes. All experiment data were processed using personal computers.

The aluminum plate used in the experiment was modified to be superhydrophobic before the experiment. The modification method is described in a previous study [52]. The purpose of this experiment is to obtain data for validation of the mathematical model.

## IV. RESULTS AND DISCUSSION

### A. Model validation

In this section, the proposed model is validated based on experimental results. Experiment data from a previous study [8] and present experiment setup were used in the validation process. In order to compare the results with previous studies [8], the computational domain for the model validation is shown in Fig. 7. The setup of computational domain is similar to Ref. [4,53]. The length and width of the rectangular computational domain are  $l_x$  and  $l_y$ , respectively. The lattice size of computational is  $N_x \times N_y$ . Humid air entered through the left inlet with a temperature  $T_a$ , humid air velocity  $u_0$ , and humidity  $W_{v,0}$  ( $x = 0$ ,  $0 \leq y \leq l_y$ ), and exited via the right outlet. An outflow boundary was applied at the outlet ( $x = l_x$ ,  $0 \leq y \leq l_y$ ). The upper surface ( $0 \leq x \leq l_x$ ,  $y = l_y$ ) and the inlet of the lower surface ( $0 \leq x < l_{x1}$ ,  $y = 0$ ) were set as adiabatic walls. The rest of the lower surface ( $l_{x1} \leq x \leq l_x$ ,  $y = 0$ ) was set as a cold wall with a constant temperature  $T_w$ , which was lower than the dew point. In all the frosting simulations in the study, the effective thermal conductivity  $\lambda_e$  of the frost layer, was calculated using the empirical correlation proposed by Yonko *et al.* [54]:

$$\lambda_e = 0.024\ 248 + 7.2311 \times 10^{-4} \rho_f + 1.183 \times 10^{-6} \rho_f^2, \quad (55)$$

where  $\rho_f$  is the density of the frost layer, which can be calculated as follows:

$$\rho_f = f_s \times \rho_s + f_a \times \rho_a. \quad (56)$$

TABLE II. Simulation parameters for case 1.

No.	Simulation parameters	Source
Case 1	$T_w = -19.5$ °C, $T_a = 21.4$ °C, $W_{v,0} = 0.0062$ kg/kg, $u_0 = 0.6$ m/s, $l_x = 140$ mm, $l_y = 10$ mm, $l_{x1} = 20$ mm; Smooth surface: $\theta_i = 77^\circ$ $N_x \times N_y = 1400 \times 100$	Ref. [8]



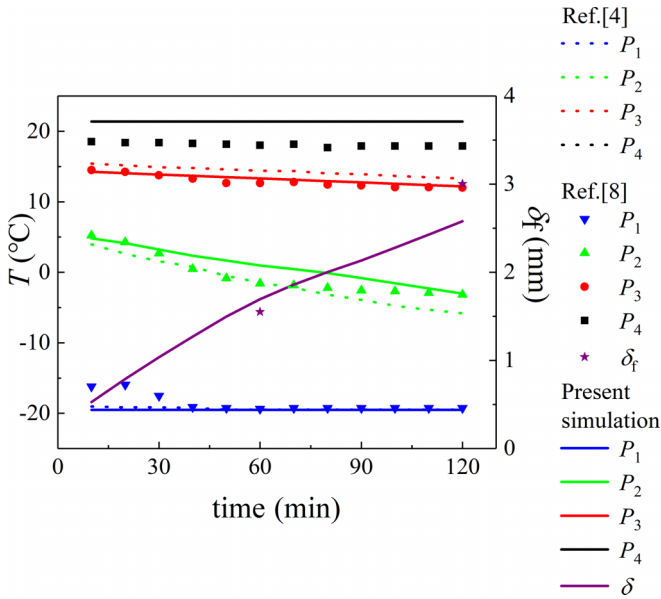


FIG. 8. Comparison of simulation results with experimental data in Ref. [8].

Furthermore, two validation cases were implemented to compare with previous studies [4,8] and present experiment, respectively. The physical properties of air, ice, and water vapor are summarized in Table I. In the modeling, lattice units were used. The lattice units can be converted from physical units according to Appendix A in the Supplemental Material [55].

1. Frosting on smooth surface

Case 1 was used to compare with previous studies [4,8]. In Ref. [8], the frosting experiment was performed on an aluminum sheet and the intrinsic contact angle was set to 77°. Since the contact angle has not been reported in previous studies [8], this contact angle was measured by a contact-angle meter. The roughness distribution of an unmodified aluminum sheet was measured via confocal laser scanning microscopy (CLSM). However, the mean roughness was less than 10–9 m, which is negligible compared to the domain size in this study. Thus, the unmodified aluminum sheets were considered to be smooth surfaces. The specific parameters for case 1 are shown in Table II.

In case 1, for comparison with the experimental results in Ref. [8] and numerical results in Ref. [4], the variation in frost thickness  $\delta_f$  and temperature within 120 min of frost

TABLE III. Relative errors between experimental data and numerical simulation for case 1.

		Error in temperature	Error in frost thickness
Case 1	$P_1$	0.36%	11.68%
	$P_2$	0.46%	
	$P_3$	0.11%	
	$P_4$	1.13%	

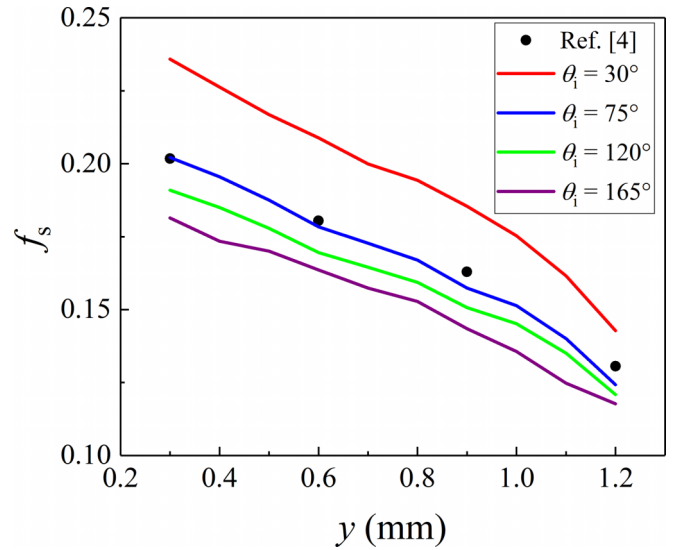


FIG. 9. Variations of ice-volume fractions along the height at  $x = 26$  mm and  $t = 60$  min.

occurrence were calculated. The frost thickness was calculated at  $x = 130$  mm, and the temperature was calculated at four different heights:  $P_1$  ( $y = 0$  mm),  $P_2$  ( $y = 3$  mm),  $P_3$  ( $y = 6$  mm), and  $P_4$  ( $y = 9$  mm). Comparisons between the present simulation and previous studies are shown in Fig. 8.

From Fig. 8, it is evident that the results of the numerical simulation are in good agreement with the previous studies. It should be noted that the results of present simulation are coincident with the results from Ref. [4] at  $P_4$ . The relative errors between numerical models with experimental data in Ref. [8] are listed in Table III. The error is obtained by calculating the average error at the specific location during the entire frosting time.

As shown in Table III, the results indicate that the proposed mathematical model can accurately predict the frosting pro-

Sk = 0.426, K = 3.993  
Rq = 1.570  $\mu$ m

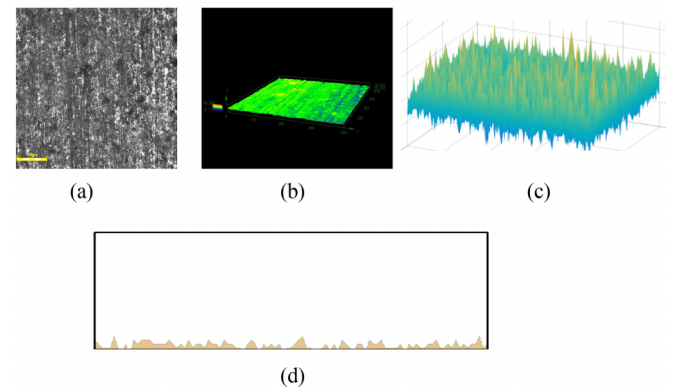


FIG. 10. Results of CLSM for the determination of roughness and numerical reconstruction of the superhydrophobic surface: (a) vertical view of CLSM result; (b) 3D surface topography obtained via CLSM; (c) 3D surface topography obtained via numerical reconstruction; and (d) 2D computational domain after numerical reconstruction.

TABLE IV. Simulation parameters for case 2.

No.	Simulation parameters	Source
Case 2	$T_w = -9\text{ }^\circ\text{C}$ , $T_a = 24\text{ }^\circ\text{C}$ , $W_{v,0} = 0.0117\text{ kg/kg}$ , $u_0 = 0.33\text{ m/s}$ , $l_x = 20\text{ mm}$ , $l_y = 5\text{ mm}$ , $l_{x1} = 0\text{ mm}$ ; rough surface: $\theta_i = 142^\circ$ , $\theta_a = 161^\circ$ $N_x \times N_y = 1000 \times 250$	Present experiment

cess. The prediction error of temperature during the frosting process is within 2%, and the prediction error of frost thickness during frost growth is within 12%. The accuracy is the same as that of other models proposed in previous studies [4,9,11].

Moreover, the frosting processes on cold surfaces with four different intrinsic contact angles were investigated to clarify the presented model, which is unique in that it can predict the frosting processes on cold surfaces with different wettabilities. The simulation parameters are listed Table II, but four different intrinsic contact angles ( $30^\circ$ ,  $75^\circ$ ,  $120^\circ$ , and  $165^\circ$ ) were implemented. The variations of ice-volume fractions along the height at  $x = 26\text{ mm}$  and  $t = 60\text{ min}$  are shown in Fig. 9. It can be seen that intrinsic contact angle  $\theta_i = 75^\circ$  gave a best fit to replicate the frosting phenomenon from Ref. [4], which is very close to the contact angle ( $\theta_i = 77^\circ$ ) measured in advance for the plate. The ice-volume fraction distributions of Ref. [4] were obtained from contour plot in Ref. [4] by MATLAB image processing.

2. Frosting on rough surface

In case 2, the comparison between the present experiment and numerical results was evaluated. It should be noted that the modified superhydrophobic aluminum surface in case 2 has some degree of roughness, and the influence of this roughness will be considered in the validation process. The roughness of the modified aluminum surface was obtained via CLSM, and was described by Sk, K, and Rq. Based on these parameters, a rough surface was reconstructed and introduced into the simulation. In present simulation, the scheme pro-

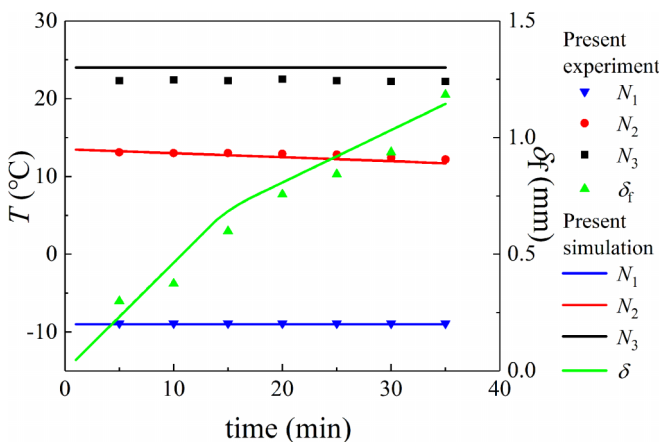


FIG. 11. Comparison of simulation results with the experimental results of this study.

TABLE V. Relative errors between experimental data and numerical simulation for case 2.

		Error in temperature	Error in frost thickness
Case 2	$N_1$	0.03%	12.85%
	$N_2$	0.12%	
	$N_3$	0.57%	

posed by Yan *et al.* [56] was used to treat the boundary on rough surface, which has second-order accuracy. The results of CLSM and numerical reconstruction in case 2 can be seen in Fig. 10.

Then, the specific parameters for case 2 are shown in Table IV.

In this, the frost thickness was calculated at  $x = 10\text{ mm}$ , and the temperature was calculated at three different heights:  $N_1$  ( $y = 0\text{ mm}$ ),  $N_2$  ( $y = 1\text{ mm}$ ), and  $N_3$  ( $y = 3\text{ mm}$ ). In present experiment, the frost morphology and frost temperature were obtained by taking pictures by high-speed camera and infrared camera, respectively, facing the flank of channel. These pictures are the two-dimensional  $x - y$  picture of the duct. It is symmetric in the  $z$  direction. So, the frost is identical in the  $z$  direction. Therefore, the 2D computational domain was employed in this validation case. Subsequently, the pictures were postprocessed in MATLAB image processing. Comparisons between the numerical simulation and experimental results are shown in Fig. 11.

The relative errors between the simulation results and the experiments are listed in Table V. The prediction errors of temperature and frost thickness are acceptable. It can be seen that the present model can also predict the frosting phenomenon on cold surface with rough structures.

Further, the frost-layer height distributions of simulation and experiment at time instants  $t = 15\text{ min}$  and  $t = 30\text{ min}$  were compared. As shown in Fig. 12, the frost-layer height distributions given by the present model are in good agreement with those from the experimental data. It should be noted that the scale of Fig. 12 was adjusted for clarity of observation. Then, the present model to predict frosting processes was well verified.

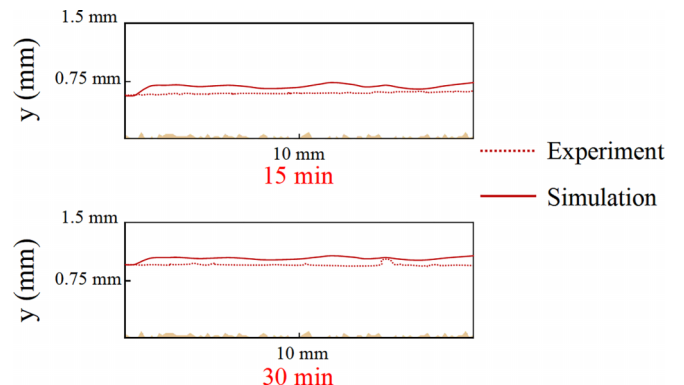


FIG. 12. Comparison of the frost-layer height distributions between simulation and experiment.

TABLE VI. Relative error of frost thickness at different position.

	$x = 2.5$ mm	$x = 5$ mm	$x = 7.5$ mm	$x = 10$ mm	$x = 12.5$ mm	$x = 15$ mm	$x = 17.5$ mm
Error	10.58%	12.29%	9.87%	12.85%	13.15%	11.31%	11.98%

Moreover, the sensitivity of the simulation error to the location of frosting was analyzed, and the error of frost thickness for seven different positions on cold surface was contrasted ( $x = 2.5, 5, 7.5, 10, 12.5, 15,$  and  $17.5$  mm). The error of different position was obtained by the average of multiple time points during the frosting process. The error of frost thickness during the frosting process is recorded in Table VI. As shown in Table VI, the error of each position is within an acceptable range, which further validates the reliability of the present model.

### B. Frosting phenomena on cold plates

In this section, the general phenomenon of the frosting process on cold plates with different wettabilities is investigated using the validated model. The computational domain and boundary conditions are shown in Fig. 7. The geometric and physical parameters used in the simulation are listed in Table VII. Both smooth and rough surfaces were considered in the simulations. The velocity and temperature fields were calculated to a steady state (approximately 50 000 time steps to a residual less than  $10^{-6}$ ) before the frosting process was initiated. For efficiency, all simulations were performed in parallel on a high-performance computer with 96 cores.

Before further research, the grid-independent test was implemented to ensure the selected grid was reliable. For case 3, three grids of sizes  $N_x \times N_y = 500 \times 50, 1000 \times 100,$  and  $1500 \times 500$  were applied to simulate the frosting process on smooth surface with  $\theta_i = 150^\circ$ ; the typical transverse distribution of temperature at  $x = 20$  mm (where the change is large) and  $t = 10$  min (when the frost growth is rapid), is presented in Fig. 13(a). For case 4, three grids of sizes  $N_x \times N_y = 500 \times 100, 1000 \times 200,$  and  $2000 \times 400$  were applied to simulate the frosting process on rough surface with  $Sk = 0, K = 3,$  and  $Rq = 1.5 \mu\text{m}$ ; the transverse distribution of temperature at  $x = 20$  mm and  $t = 10$  min is presented in Fig. 13(b). It can be seen that the present grids ( $1000 \times 100$  and  $1000 \times 200$ ) are fine enough to obtain grid-independent

solutions, which means that the present grids can be applied to the following studies.

Subsequently, a smooth surface was first modeled. The distribution of the ice-volume fraction and temperature for case 3 are shown in Fig. 14. Only two typical conditions ( $\theta_i = 60^\circ, 150^\circ$ ) for the horizontal zone of  $8 \text{ mm} \leq x \leq 50 \text{ mm}$  are shown for convenience.

From Fig. 14, it is evident that the frost-layer thickness and ice-volume fraction increase simultaneously over time. A high ice-volume fraction always appears at the leading part of the frost layer, which has been reported many times in previous studies [4,9]. The temperature in the entire zone decreases and the temperature at the same position decreases with time, which is consistent with the findings of previous studies [4,11].

The average thickness and average density of the frost layer were used to characterize its properties. They can be defined as follows:

$$\delta_{\text{ave}} = \frac{\sum_{l_{x1}}^{l_x} \delta_f}{l_x - l_{x1}}, \quad (57)$$

$$\rho_{\text{ave}} = \frac{\sum_{l_{x1}}^{l_x} \rho_f}{l_x - l_{x1}}. \quad (58)$$

The average frost-layer thickness and average frost-layer density on the smooth cold plates with different intrinsic contact angles are shown in Fig. 15 after 60 min of frosting. It is evident that for an increase in the surface intrinsic contact angle, there is little difference in the frosting thickness, whereas the frosting thickness on the hydrophobic surface increases slightly. The average density of the frost layer on the hydrophobic surface was significantly less than that on the hydrophilic surface. The frost density can be significantly reduced by slightly increasing the intrinsic contact angle on the hydrophilic surface. However, this parameter was not significantly reduced by increasing the intrinsic contact angle on the hydrophobic surface. The frosting density on the cold plate at  $\theta_i = 150^\circ$  was 34.7% less than that on a plate with  $\theta_i = 30^\circ$ .

TABLE VII. Simulation parameters for the frosting process with different wettability.

No.	Parameters	Intrinsic contact angle	Roughness
Case 3	$T_w = -20^\circ\text{C}, T_a = 10^\circ\text{C}, W_{v,0} = 0.006 \text{ kg/kg}, u_0 = 0.5 \text{ m/s},$ $l_x = 50 \text{ mm}, l_y = 5 \text{ mm}, l_{x1} = 10 \text{ mm}$ $N_x \times N_y = 1000 \times 100$	$30^\circ - 150^\circ$	Smooth
Case 4	$T_w = -20^\circ\text{C}, T_a = 10^\circ\text{C}, W_{v,0} = 0.006 \text{ kg/kg}, u_0 = 0.5 \text{ m/s},$ $l_x = 50 \text{ mm}, l_y = 10 \text{ mm}, l_{x1} = 0 \text{ mm}$ $N_x \times N_y = 1000 \times 200$	$140^\circ$	$Sk = -1 - 1$ $K = 2 - 4$ $Rq = 1.0 - 2.0 \mu\text{m}$

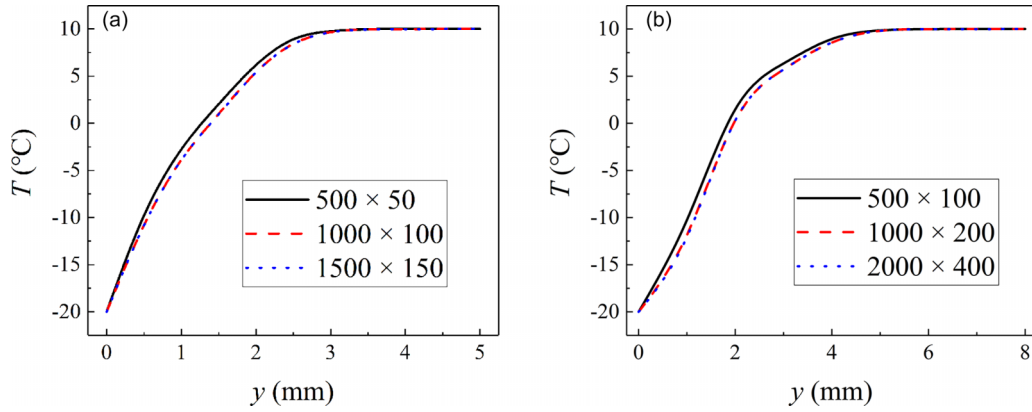


FIG. 13. Grid-independent test for case 3 and case 4.

Roughness has a compound effect on wettability. It has previously been observed that typical superhydrophobic surfaces have randomly distributed rough structures [52]. Therefore, the effects of roughness on the frosting process of superhydrophobic surfaces should be investigated further.

The instantaneous distribution of the ice-volume fraction and temperature in case 4 are shown in Fig. 16. A typical Gaussian random roughness ( $Sk = 0$ ,  $K = 3$ ,  $Rq = 1.5 \mu\text{m}$ ,  $\theta_i = 140^\circ$ , and  $\theta_a = 155.5^\circ$ ) was considered. Similar to the frosting process on a smooth surface, the frost-layer thickness and ice-volume fraction both increase over time. Likewise, the temperature in the entire zone decreases, and the temperature

at the same position decreases with time. Furthermore, ice tends to accumulate at concave points with random roughness. According to the classical heterogeneous nucleation theory [57], this phenomenon is caused by the presence of inhomogeneous local surface energy. On the concave points, the critical nuclei are smaller than the critical nuclei on a flat or convex surface, which results in a lower nucleation barrier [57]. Moreover, as the concave points become sharper, the nucleation barrier exhibits a monotonic decline. This conclusion was confirmed by molecular dynamics simulations [58].

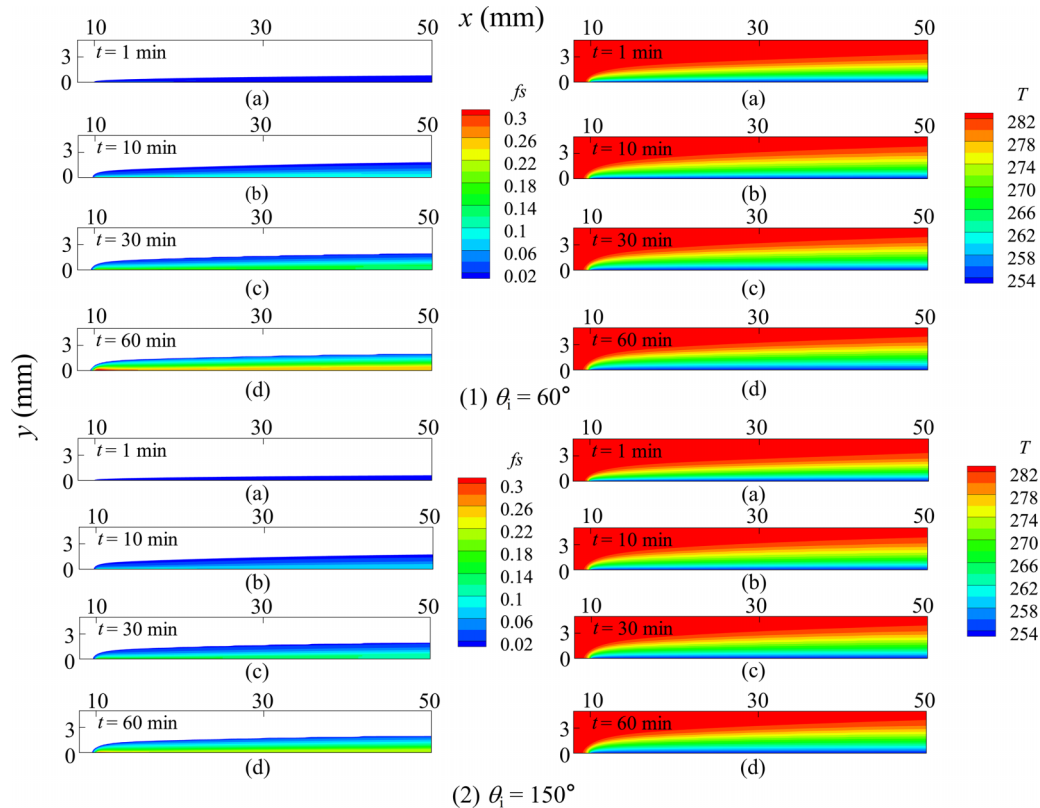


FIG. 14. Ice-volume fraction and temperature distributions during the frosting process on smooth cold surfaces with two different intrinsic contact angles ( $60^\circ$  and  $150^\circ$ ) at time instants  $t = 1, 10, 30,$  and  $60$  min from (a) to (d).

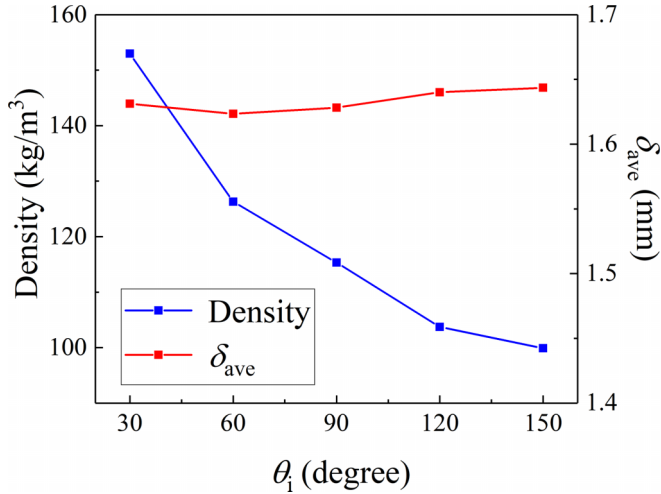


FIG. 15. Frosting density and frosting thickness on smooth cold surfaces with different intrinsic contact angles.

The average frost-layer thickness and density on the cold plates after 60 min of frosting are shown in Fig. 17 for different roughness parameters.

From Fig. 17, it is evident that the frosting thickness is seldom influenced by the roughness parameters. The frosting density can increase significantly by increasing  $K$  and  $Rq$ , but decreases significantly with increasing  $Sk$ . This behavior can be attributed to the concave points on the surface. The more concave points that exist on the surface, the more active nucleation sites are available for phase changes, thereby increasing the frosting density. This finding can provide insights into the design of antifrosting surfaces.

### C. Frosting phenomena in microchannels

Currently, superhydrophobic surfaces are used in microchannel heat exchangers for antidust purposes. Frosting behavior is investigated in this study using the proposed model. As shown in Fig. 18, a simplification is made in that

TABLE VIII. Geometric parameters of the microchannel.

Parameters	Values (mm)
Depth	25.4
Height	8.1
Width	3.4

the stack of fins is considered as triangular. Furthermore, a single triangular channel was modeled for saving simulation time. The key geometric parameters of the microchannel are listed in Table VIII. The grid of sizes  $N_x \times N_y \times N_z = 508 \times 68 \times 162$  was employed in present study. The single-mesh size is  $50 \mu\text{m} \times 50 \mu\text{m} \times 50 \mu\text{m}$  in physical units. In summary, the physical parameters are as follows:  $T_a = 2^\circ\text{C}$ ,  $T_w = -10^\circ\text{C}$ ,  $u_0 = 0.5 \text{ m/s}$ , and  $W_{v,0} = 0.004 \text{ kg/kg}$ .

Before the further research of frosting process in the microchannel, the grid-independent test was implemented to ensure the selected grid was reliable. Three grids of sizes  $N_x \times N_y \times N_z = 254 \times 34 \times 81$ ,  $508 \times 68 \times 162$ , and  $762 \times 102 \times 243$  were applied to simulate the frosting process in microchannel. The average density of frost layer at different time is recorded in Fig. 19. As shown in Fig. 19, the present grids ( $508 \times 68 \times 162$ ) were fine enough to obtain grid-independent solutions and can be used in the following research.

For a qualitative comparison, a typical superhydrophobic microchannel with  $\theta_a = 153^\circ$ ,  $\theta_i = 124^\circ$ ,  $Sk = 0.579$ ,  $K = 3.062$ , and  $Rq = 8.981 \mu\text{m}$  was prepared for the frosting experiment. The frosting experiment and numerical simulation of the microchannel were performed simultaneously. The numerically reconstructed rough surfaces of the microchannels are shown in Fig. 20.

Figure 21(a) shows the distribution of the ice-volume fraction during the frosting process in the superhydrophobic microchannel. A cross section of  $x = 12 \text{ mm}$  is plotted at two time intervals ( $t = 10$  and  $30 \text{ min}$ ). Further, the frost morphol-

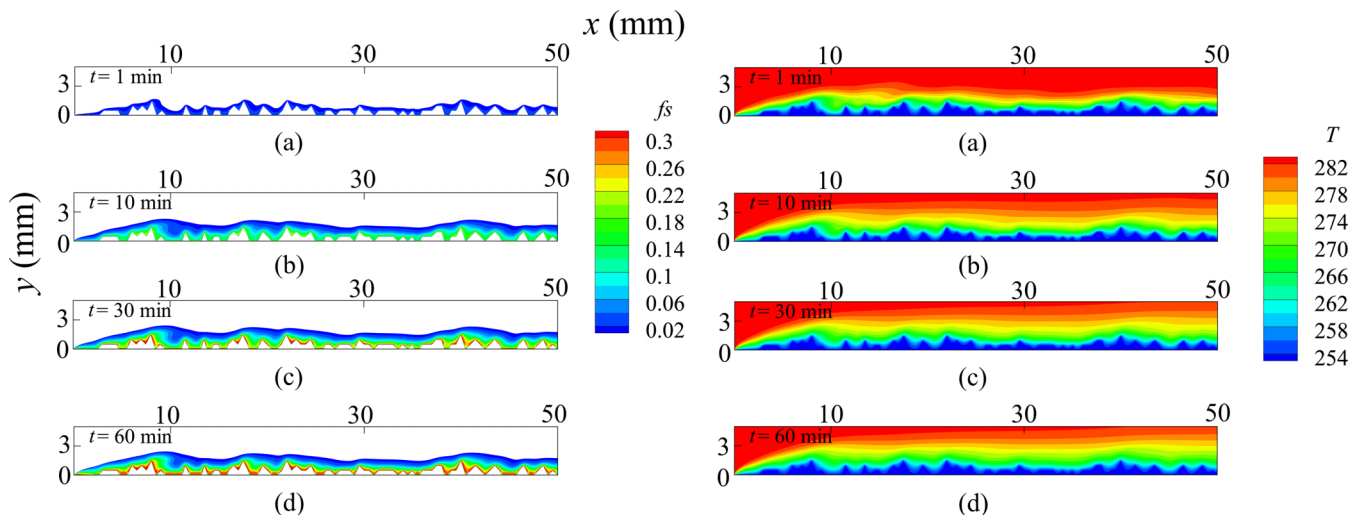


FIG. 16. Ice-volume fraction and temperature distributions of frosting process on a cold coarse surface with Gaussian random roughness and  $\theta_i = 140^\circ$  and  $\theta_a = 155.5^\circ$  at time instants  $t = 1, 10, 30$ , and  $60 \text{ min}$  from (a) to (d).

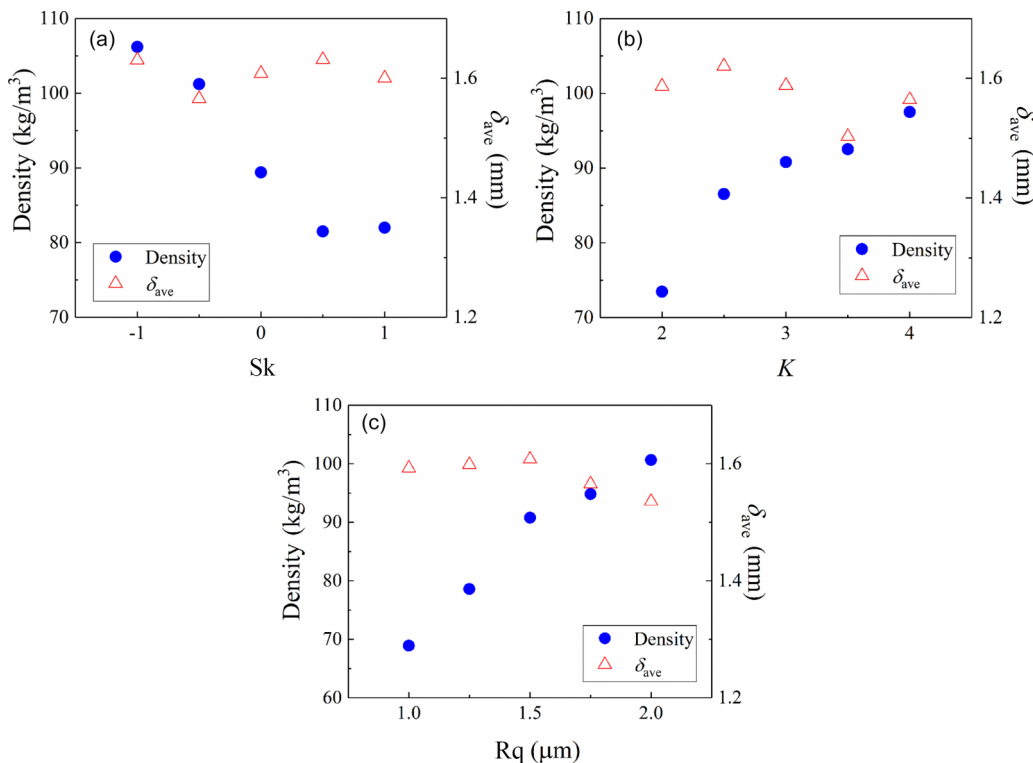


FIG. 17. Frosting density and frosting thickness on cold surfaces after 60 min frosting for different roughness parameters: (a) Effects of Sk with  $K = 3.0$  and  $Rq = 1.5 \mu\text{m}$  (b) effects of K with  $Sk = 0.0$  and  $Rq = 1.5 \mu\text{m}$  (c) effects of Rq with  $Sk = 0.0$  and  $K = 3.0$ .

ogy in the microchannel during the experiment is shown in Fig. 21(b).

As shown in Fig. 21, the same growth pattern can be observed in the simulation and the experiment. The frost layer first grows along the fins and then toward the inside of the channel, which leads to the increase of flow resistance and the

decrease of heat-transfer efficiency. Similar to the frosting on the plate, the volume fraction of ice also increases with time in the microchannel. At the initial stage of frosting process, the frost on the fin is relatively loose, and then the more dense frost layer can be observed with the extension of frosting time.

Furthermore, the effects of the intrinsic contact angles on the frosting processes in the microchannels were investigated. These effects are represented by the frosting mass  $m_f$ , which

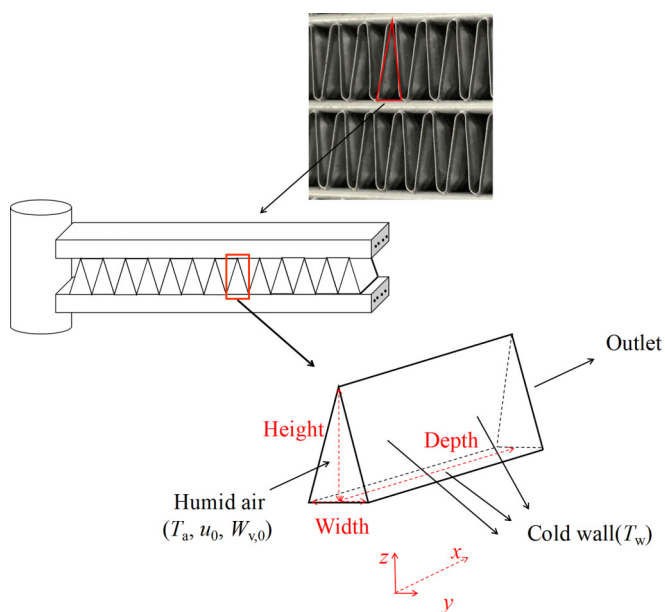


FIG. 18. Computational domain for frosting phenomena in the microchannel.

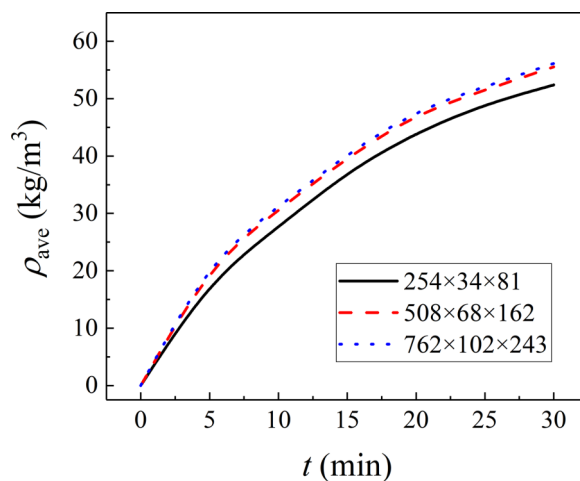


FIG. 19. Grid-independent test for the simulation of frosting process in the microchannel.

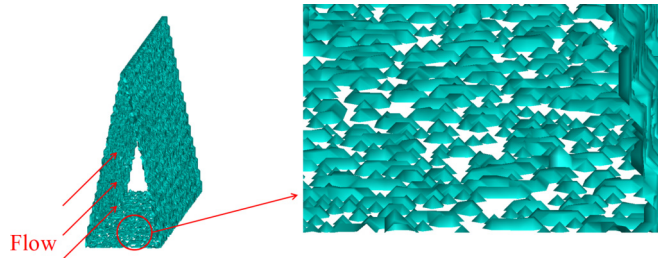


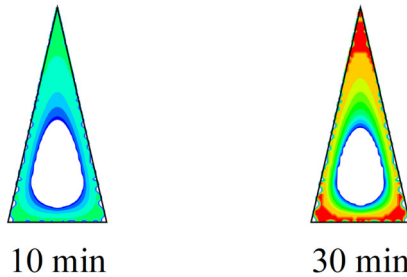
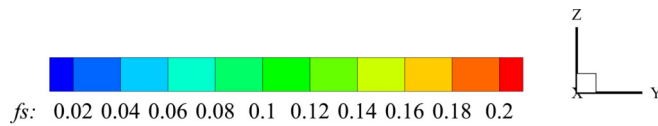
FIG. 20. Numerically reconstructed rough surfaces of the microchannels.

can be defined as

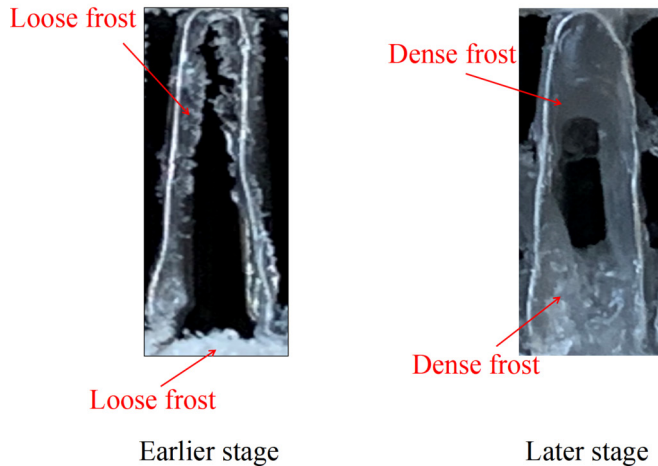
$$m_f = \rho_{ave} V_{grid} \tag{59}$$

where  $V_{grid}$  is the volume of all frosting computational grids.

The frosting mass in the microchannels with different intrinsic contact angles of frosting is shown in Fig. 22 after 30 min. It was determined that the frosting mass on a hydrophilic microchannel was higher than that on a hydrophobic microchannel. This phenomenon has been reported in a previous experimental study [59]. Under the frosting conditions



(a) Distribution of the ice volume fraction based on the numerical simulation



(b) The frost morphology in the microchannel during the experiment

FIG. 21. Results of numerical and observed frosting thickness in the microchannel.

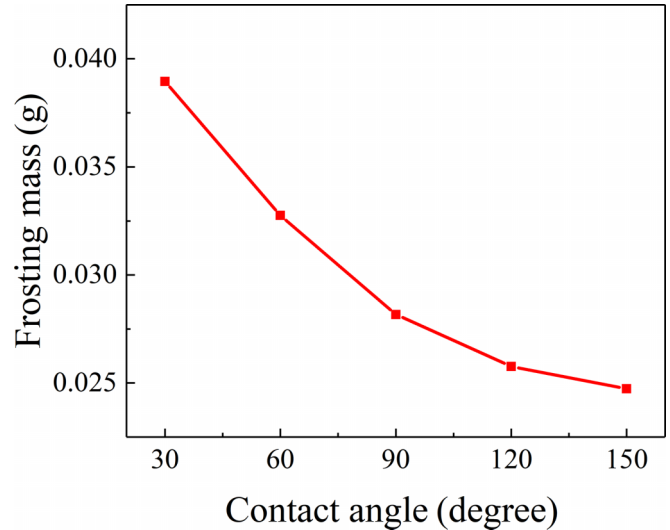


FIG. 22. Frosting mass in microchannels with different intrinsic contact angles after the frosting process.

used in the simulation, the frosting mass of the microchannel with  $\theta_i = 125^\circ$  was 35.3% less than that with  $\theta_i = 55^\circ$ . In summary, decreasing the wettability of microchannels can also inhibit frost formation and growth. The cause can be divided into two components: first, nucleation on hydrophobic surfaces is associated with a higher interfacial free energy and thus increases the nucleation barrier [30]. Second, the formation of fewer ice crystals on the hydrophobic surface due to the greater nucleation barrier of the nucleation process, which results in dwarf frost crystals on the hydrophobic surface relative to that on the hydrophilic surface. From Fig. 23, it is evident that the dwarf frost crystals on the hydrophobic surface result in a higher curvature radius  $r_{cu}$  of ice nuclei on hydrophobic surfaces compared to those on hydrophilic surfaces. According to the Gibbs-Thomson effect [30], the degree of supercooling caused by the curvature of ice nuclei on hydrophobic surfaces is lower than the degree of supercooling caused by the curvature on hydrophilic surfaces, which results in slow dendrite growth on the former.

### V. CONCLUSIONS

In this study, a lattice Boltzmann model for predicting frosting processes on cold surfaces with different wettabilities was proposed. The governing equations for mass transfer between moist air and the ice phase were established based

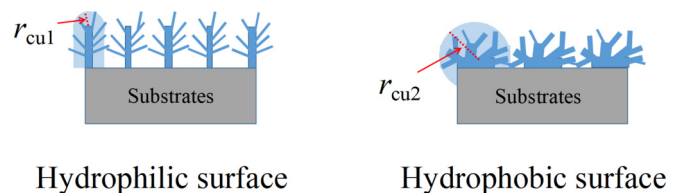


FIG. 23. Schematic of dendrites growth on a cold surface with different wettability.

on the heterogeneous nucleation and crystal growth theories. The effects of the contact angle and roughness of the surfaces were considered. An experimental setup for frost formation and growth was used to observe the frosting phenomenon and to validate the model. The accuracy of the model was found to be acceptable. Then, the frosting processes on cold plates and in microchannels with different contact angles and rough structures were investigated to gain insight into the frosting behavior on supercooled surfaces with different wettability. The main conclusions are as follows:

(1) For frosting processes on smooth cold surfaces, the distribution of the ice-volume fraction and temperature field is similar to that obtained in previous studies without considering wettability.

(2) For frosting processes on smooth cold surfaces with different intrinsic contact angles, the frost thickness at a given frosting time is similar. However, the frost density on a hydrophobic plate is significantly less than that on a hydrophilic plate. Under the frosting conditions in this study, the frosting density on a cold plate with an intrinsic contact angle of  $150^\circ$  was 34.7% less than that on a plate with an intrinsic contact angle of  $30^\circ$ .

(3) For frosting processes on rough cold surfaces, the concave points in the roughness could increase the number of sites for active nucleation where icing is more prone to occur. Therefore, a larger skewness, smaller kurtosis, and smaller standard deviation will lead to fewer concave points, which result in decreased frosting. This has implications for the design of antifrost rough structures.

(4) The frosting mass in the hydrophobic microchannel was significantly lower than that in the hydrophilic microchannel. Under the frosting conditions in this study, the frosting mass in a microchannel with an intrinsic contact angle of  $125^\circ$  was 35.3% less than that with an intrinsic contact angle of  $55^\circ$ .

(5) Hydrophobic modification and appropriate design of rough surface structures can be effective in minimizing the damage caused by frosting.

#### ACKNOWLEDGMENTS

This project was supported by the Natural Science Foundation of China (Grant No. 51936005). It was also supported by the research project from Sanhua Holding Group.

- 
- [1] W. Sheng, P. P. Liu, C. B. Dang, and G. X. Liu, *Renew. Sust. Energ. Rev.* **79**, 806 (2017).
- [2] A. Leoni, M. Mondot, F. Durier, R. Revellin, and P. Haberschill, *Int. J. Refrig.* **68**, 198 (2016).
- [3] M. J. Song and C. B. Dang, *Int. J. Heat Mass Transfer* **124**, 586 (2018).
- [4] T. M. Lei, K. H. Luo, and D. Wu, *Phys. Rev. E* **99**, 053301 (2019).
- [5] K. S. Lee, W. S. Kim, and T. H. Lee, *Int. J. Heat Mass Transfer* **40**, 4359 (1997).
- [6] B. Na and R. L. Webb, *Int. J. Heat Mass Transfer* **47**, 925 (2004).
- [7] K. Lenic, A. Trp, and B. Frankovic, *Appl. Therm. Eng.* **29**, 2534 (2009).
- [8] K. Lenic, A. Trp, and B. Frankovic, *Int. J. Heat Mass Transfer* **52**, 22 (2009).
- [9] J. M. Armengol, C. T. Salinas, J. Xaman, and K. A. R. Ismail, *Int. J. Therm. Sci.* **104**, 245 (2016).
- [10] D. Kim, C. Kim, and K. S. Lee, *Int. J. Heat Mass Transfer* **82**, 135 (2015).
- [11] X. M. Wu, Q. Ma, F. Q. Chu, and S. Hu, *Int. J. Heat Mass Transfer* **96**, 11 (2016).
- [12] X. M. Wu, F. Q. Chu, Q. Ma, and B. Zhu, *Appl. Therm. Eng.* **118**, 448 (2017).
- [13] Y. C. Shen, H. Y. Zou, and S. Wang, *Langmuir* **36**, 13563 (2020).
- [14] Y. Zhao, Z. Yan, H. Zhang, C. Yang, and P. Cheng, *Int. J. Heat Mass Transfer* **165**, 120609 (2021).
- [15] C. Reichl, C. Sandstrom, F. Hochwallner, F. Linhardt, M. Popovac, and J. Emhofer, *Appl. Therm. Eng.* **199**, 117487 (2021).
- [16] S. M. Li and C. C. Wang, *Int. Commun. Heat Mass* **129**, 105670 (2021).
- [17] S. S. Feng, J. J. Kuang, T. Wen, T. J. Lu, and K. Ichimiya, *Int. J. Heat Mass Transfer* **77**, 1063 (2014).
- [18] S. S. Feng, Y. Zhang, M. Shi, T. Wen, and T. J. Lu, *Appl. Therm. Eng.* **88**, 315 (2015).
- [19] M. Sheikholeslami, *J. Mol. Liq.* **265**, 347 (2018).
- [20] Z. L. Guo and T. S. Zhao, *Phys. Rev. E* **66**, 036304 (2002).
- [21] A. Faghri, Y. W. Zhang, and J. Howell, *Advanced Heat and Mass Transfer* (Global Digital Press, Columbia, MO, 2010).
- [22] S. Ergun, *Chem. Eng. Prog.* **48**, 89 (1952).
- [23] K. Vafai, *J. Fluid. Mech.* **147**, 233 (1984).
- [24] Y. Hayashi, A. Aoki, S. Adachi, and K. Hori, *ASME J. Heat Mass Transfer* **99**, 239 (1977).
- [25] M. H. Kim, H. Kim, K. S. Lee, and D. R. Kim, *Energ. Convers. Manage.* **138**, 1 (2017).
- [26] J. Cui, W. Z. Li, Y. Liu, and Y. S. Zhao, *Int. J. Heat Fluid Flow* **32**, 249 (2011).
- [27] J. Cui, W. Z. Li, Y. Liu, and Z. Y. Jiang, *Appl. Therm. Eng.* **31**, 447 (2011).
- [28] Y. M. Liu, Z. L. Liu, L. Y. Huang, and J. F. Sun, *Sci. China Technol. SC* **53**, 807 (2010).
- [29] J. Y. Gong, J. Q. Hou, G. J. Li, T. Y. Gao, and J. J. Sun, *Int. Commun. Heat Mass* **98**, 116 (2018).
- [30] Z. S. Zhang and X. Y. Liu, *Chem. Soc. Rev.* **47**, 7116 (2018).
- [31] S. Zeng, Q. W. Su, and L. Z. Zhang, *Int. J. Heat Mass Transfer* **152**, 119508 (2020).
- [32] S. Kim and K. J. Kim, *ASME J. Heat Mass Transfer* **133**, 081502 (2011).
- [33] J. E. McDonald, *Am. J. Phys.* **31**, 31 (1963).
- [34] A. G. Gerber and M. J. Kermani, *Int. J. Heat Mass Transfer* **47**, 2217 (2004).
- [35] N. Sharifi, *Int. J. Mech. Sci.* **165**, 105221 (2020).



- [36] O. Funke, G. Phanikumar, P. K. Galenko, L. Chernova, S. Reutzel, M. Kolbe, and D. M. Herlach, *J. Cryst. Growth* **297**, 211 (2006).
- [37] D. D. Zhao, J. R. Gao, and A. Kao, *Int. J. Heat Mass Transfer* **159**, 120113 (2020).
- [38] Y. Zhao, Q. Guo, T. Lin, and P. Cheng, *Int. J. Heat Mass Transfer* **159**, 120074 (2020).
- [39] F. Wang, Study on mechanism and characteristics of frosting and defrosting on superhydrophobic fin surface, Ph.D. thesis, Southeast University, 2017.
- [40] J. Lipton, M. E. Glicksman, and W. Kurz, *Mater. Sci. Eng.* **65**, 57 (1984).
- [41] J. Lipton, W. Kurz, and R. Trivedi, *Acta Metallurgica* **35**, 957 (1987).
- [42] F. Wang, C. H. Liang, and X. S. Zhang, *Renew. Sust. Energ. Rev.* **81**, 707 (2018).
- [43] Z. L. Guo and C. Chu, *Lattice Boltzmann Method and Its Applications in Engineers* (World Scientific, Singapore, 2013).
- [44] T. Kruger, H. Kusumaatmaja, A. Kuzmin, O. Shardt, G. Silva, and E. M. Viggen, *The Lattice Boltzmann Method Principles and Practice* (Springer, Switzerland, 2017).
- [45] D. R. Noble and J. R. Torczynski, *Int. J. Mod. Phys. C* **9**, 1189 (1998).
- [46] C. Y. Zhang, H. Zhang, W. Z. Fang, Y. G. Zhao, and C. Yang, *Phys. Rev. E* **101**, 023314 (2020).
- [47] S. Chakraborty and D. Chatterjee, *J. Fluid Mech.* **592**, 155 (2007).
- [48] W. Wu, S. L. Zhang, and S. F. Wang, *Int. J. Heat Mass Transfer* **104**, 675 (2017).
- [49] J. J. Wu, *Tribol. Int.* **37**, 339 (2004).
- [50] K. K. Manesh, B. Ramamoorthy, and M. Singaperumal, *Wear* **268**, 1371 (2010).
- [51] W. Z. Yuan and L. Z. Zhang, *Langmuir* **33**, 820 (2017).
- [52] Y. Y. Quan and L. Z. Zhang, *Appl. Surf. Sci.* **292**, 44 (2014).
- [53] X. M. Wu, F. Q. Chu, and Q. Ma, *Int. J. Heat Mass Transfer* **110**, 760 (2017).
- [54] J. D. Yonko and C. F. Sepsy, *ASHRAE Transactions* **73**, 1.1 (1967).
- [55] See Supplemental Material at <http://link.aps.org/supplemental/10.1103/PhysRevE.107.065304> for the conversion between physical units and lattice units.
- [56] Y. Y. Yan and Y. Q. Zu, *Int. J. Heat Mass Transfer* **51**, 2519 (2008).
- [57] D. Turnbull, *J. Chem. Phys.* **18**, 198 (1950).
- [58] Y. Bi, B. Cao, and T. Li, *Nat. Commun.* **8**, 15372 (2017).
- [59] L. Pu, R. Liu, H. Huang, S. Q. Zhang, Z. G. Qi, W. D. Xu, and J. Zhou, *Energ. Build.* **226**, 110382 (2020).